ALMA MATER STUDIORUM
UNIVERSITÀ DI BOLOGNA

SCHOOL OF ENGINEERING AND ARCHITECTURE
-Forlì Campus-

SECOND CYCLE MASTERS DEGREE in
INGEGNERIA AEROSPAZIALE/AEROSPACE ENGINEERING
Class LM-20

GRADUATION THESIS
In Radio Communication and Radar Systems

Experimental Path Loss Models
for UWB Multistatic Radar Systems

CANDIDATE:

Luis Adolfo Alfaro Hidalgo

SUPERVISOR:

Enrico Paolini

CO-SUPERVISOR:

Andrea Giorgetti

ACADEMIC YEAR 2016/2017

Abstract

The use of Ultra-Wideband (UWB) radio technology in a multistatic radar system has recently gained interest to implement Wireless Sensor Networks (WSN) capable of detecting and tracking targets in indoor environments[13]. Due to the increasing attention towards multistatic UWB systems, it is important to perform the radio channel characterization. In this Thesis we focus on the characterization of the path loss exponent (α).

To perform the present work, the followed methodology was to collect experimental data from the UWB devices using a suitable target, this information was processed with a clutter removal algorithm using the Empty Room (ER) approach, then the contribution of the target was isolated to produce a graph of energy as a function of the product between the target-to-transmitter and the target-to-receiver distances in a bistatic configuration. Finally, using this plot it was properly obtained the value of the path loss exponent.

As as additional experimental result, the main statistical parameters associated to the residual clutter were calculated, which are expected to allow having a better understanding and characterization of the radar system performance in the experimental environments.

Keywords: Bistatic Radar, Channel Models, Clutter Removal, Experimental Measurements, Matlab Code, Path Loss Exponent, Residual Clutter, Ultra-Wideband (UWB)

to God for being my fortitude, to my wife and my parents for giving me all their support and help

Contents

List of Figures

List of Tables

Chapter 1

Introduction

The use of UWB radio technology in a multi-static radar system has recently gained interest to implement WSN applied to detect and track targets [4] [5] [10] [11] [12] [13]. Some of the main benefits of the UWB radar systems include their localization resolution of the order of centimeters and, due to the broad range of frequencies used in their operations, the possibility of performing detection of objects occluded by walls, furniture or other artifacts. This last reason, makes this technology ideal to be used in indoor facilities.

The indoor facilities of interest to the human activities are commonly furnished and composed by rooms of different sizes, all these objects and structures represent an obstacle for target's detection and localization, in this scenario is that the UWB technology comes to be useful and therefore a growing field of study.

As it is detailed further, the UWB equipment used during this work coherently transmits pulses between 3 GHz and 5 GHz having an RF bandwidth of 1.4 GHz. Inside this bandwidth, a specific train of pulses (using the Impulse Radio concept) is sent and the device transmits a train with a frequency of 10 MHz.

Due to the increasing attention towards multistatic UWB systems, it is important to perform radio channel characterization. In this Thesis we focus on the characterization of the path loss exponent (α), therefore this document describes the activities carried out to collect experimental data using the UWB technology, and how this information was processed to calculate α.

To accomplish the desired goal, measuring experiments were performed inside different buildings of the School of Electronics and Telecommunications of the University of Bologna in the campus of Cesena. After the data recollection was completed, a clutter removal algorithm based on previous works (as described in [14]) was modified and in conjunction with additional processing steps: the path loss exponent was calculated from the experimental data.

To properly detail the required phases to achieve the goal, this document is divided in the following sections:

- **Experiment Fundamentals and Scenario Set-Up.** This section describes the fundamental theoretical concepts associated to the present work, the equipment used to perform the tests along with the devices' main features and the configuration to perform the data acquisition. Later in the chapter, the code pipeline to process the collected data is presented together with the required file preparations to execute this code.

- **First Experiment: "Laboratory of Electronics and Telecommunications (LEle) Laboratory".** In this chapter the experimental scenario, the measuring procedure and the code process are described. Additionally, the partial and final results of the code process are presented for an example case, then the outcome is presented and analyzed. At the end of the section, statistical parameters gathered for the "residual clutter" of the scenario are shown.

- **Second Experiment: "Department of Electrical, Electronics and Information Engineering (DEI)'s Garage".** This chapter includes a scenario description (equipment and measurement points), then a brief confirmation on the process chain and the output data obtained for the garage are introduced and discussed. Finally, the statistics related to the "residual clutter" are shown along with its analysis.

- **Conclusion and Recommendations.** In this final chapter, the main achievements of the present work are recapitulated in a brief manner. Also some possible improvements that can be performed to similar works carried in the future were included.

Additionally, at the end of the document (Annex) all the points measured in the experimental scenarios are enlisted. All this information is presented in Cartesian coordinates and the origin of the entire system in each case is located in the middle point of the distance between the transmitter (TX) and receiver (RX).

Chapter 2

Experiment Fundamentals and Scenario Set-Up

2.1 Radar Basic Principles

The main goal of a radar system is to perform target detection and estimate its position (this position is calculated with respect to the location of the TX and the RX nodes). To calculate a target location, the system analyzes the signals that are received after the transmission of a specific set of pulses (in other words, the TX emits a given set of pulses then, the RX node records the signals during a time window and the data is analyzed).

The information received in the RX is used to produce an accurate approximation of different quantities according to the system's interests, for example the ToA of a specific scattered signals, scattered energy or power, etc.

For the purposes of the present work, a bistatic radar configuration is used. The main characteristics in a bistatic system are: the TX and RX positions are known; and the distance between the target and the stations is in the same order of magnitude as the separation between the equipment nodes [6] (this stations' separation is usually referred to as the baseline and denoted by L).

The bistatic configuration was selected since it provides with the necessary capabilities to isolate the contribution of a given target in the received signal at RX and the, use these waveforms to estimate the power scattered.

Using the ToA principle, all the positions in which the ToA remains constant, form an elliptical trajectory [9] for the bistatic system. This kind of curve is described in Figure 2.1 where the distance between the TX and RX is denoted by L, the distance between TX and the

target is marked as L_1 and the distance between RX and the target is set as L_2.
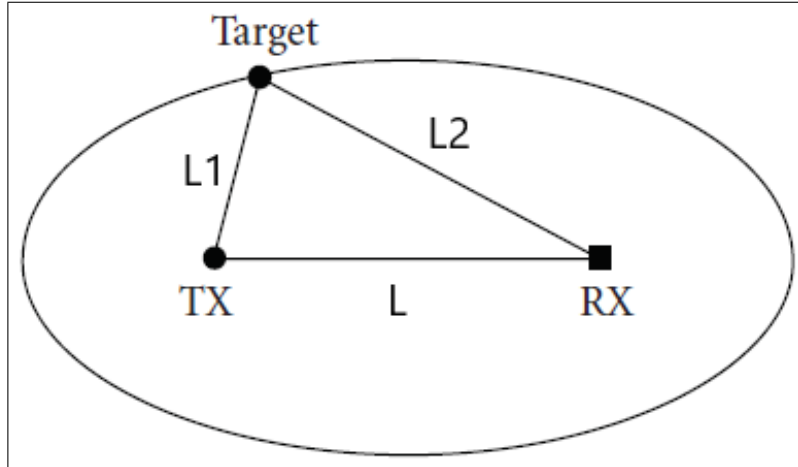
Figure 2.1: Constant ToA line of a bistatic radar. [9]

From Figure 2.1, it is clear that to determine the position of a target, it is required to have more than three receivers (for further details, refer to [15]). However, to characterize the channel by calculating the path loss exponent, it is sufficient to use a bistatic radar configuration.

At this point, it is useful to notice that there is a line in the monitored space such that at node RX, it is possible to receive an echo signal of constant power (in ideal propagation conditions). These lines are known as Cassini ovals [6] [9]. An example of such curve is presented in Figure 2.2.
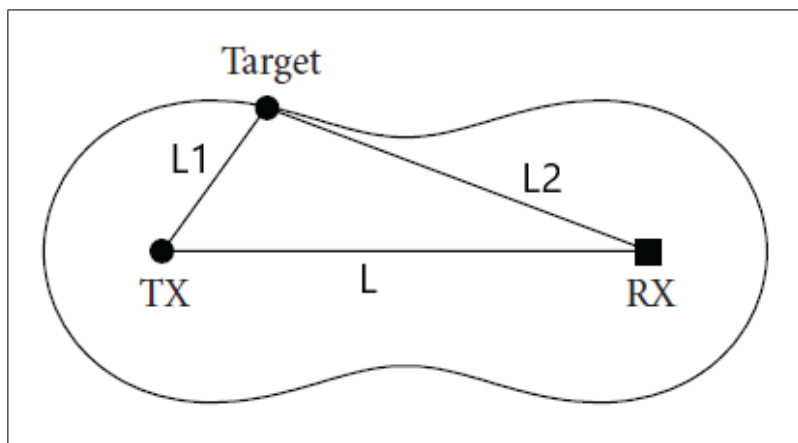
Figure 2.2: Constant Power line of a bi-static radar. [9]

In Figure 2.2 the distances denoted as L, L_1 and L_2 follow the exact definition as the previous figure where the ellipse is depicted.

An aspect of the bistatic configuration that has to be considered, is the existence of a minimum and a maximum Cassini oval in which it is possible to detect the target. In the first

case, this zone is called the "blind zone" and it is a region in the vicinity of the baseline, inside this region, the system is not able to distinguish the signal's reflected path from the direct path which as a consequence, makes detection impossible. For the second case, there is a maximum allowed separation between the target and the stations for the system to be capable of detecting the object, this is defined by the maximum Cassini oval and this region is determined by the equipment features. Both these regions are depicted in Figure 2.3.
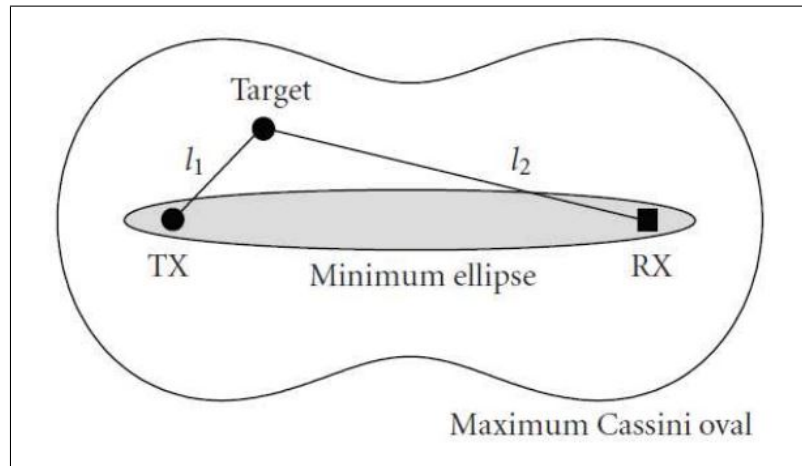
Figure 2.3: Blind zone of a bi-static radar. [14]

Additionally, from previous work [1], it is known the equation for received power due to the echo produced by a target as

$$P_r^{target} = g(f, f_L, B) \cdot (L_1 L_2)^{-\alpha} \tag{2.1}$$

where the variables correspond to:

- P_r is the received power at the RX node due to the target's echo;
- L_1 is the distance between the TX node and the target;
- L_2 corresponds to the distance between the target and the RX node;
- α is the path loss exponent;
- $g(f, f_L, B)$ is an unknown function that depends on the parameters:
    - S_t gives the one-sided transmitted power spectral density;
    - G_t corresponds to the transmitting antenna gain;
    - G_r gives the receiving antenna gain;
    - σ is the Radar Cross Section (RCS) of the target;
    - c corresponds to the speed of light;
    - f_L is the lower boundary of the signal bandwidth;
    - B is the bandwidth of the signal define in the frequency range of $[f_L, f_U]$.

From (2.1), it can be highlighted that in the case where function $g(f, f_L, B)$ remains constant, if it is possible to acquire and isolate the target's contribution in the received signal, then it is feasible to obtain an experimental value of α by calculating the received power due to the target's scattering and then plotting P_r^{target} as function of $(L_1 \cdot L_2)$.

Now, it is proper to emphasize that to perform the previous described task, all the elements of the system gathered in the term $g(f, f_L, B)$ of (2.1) must remain constant.

2.2 Discrete Signal Power

For the purposes of the present work, it is required to account for the power of a signal in the discrete time domain [8]. To calculate this quantity, it is used the relationship:

$$Power[dB] = 10 \log_{10} \left(\frac{\sum_{k=k_0}^{k_f} |x(k)|^2}{k_f - k_0 + 1} \right) \tag{2.2}$$

where:

- $x(k)$ is the array containing the discrete signal values;
- k_0 corresponds to the initial index value to calculate the power;
- k_f represents the final index used in the computation.

The values of k_0 and k_f are selected according to an estimation made of the position of the target during each experiment. This estimation is done by calculating a window of time according to the geometric relations described in Section 2.3.2. Additionally, a description of the application of this concept is included in the following sections when presenting the experimental results.

2.3 Experiment Preparations

The radar system that is used in this work is set in a bistatic configuration as presented in Figure 2.4.
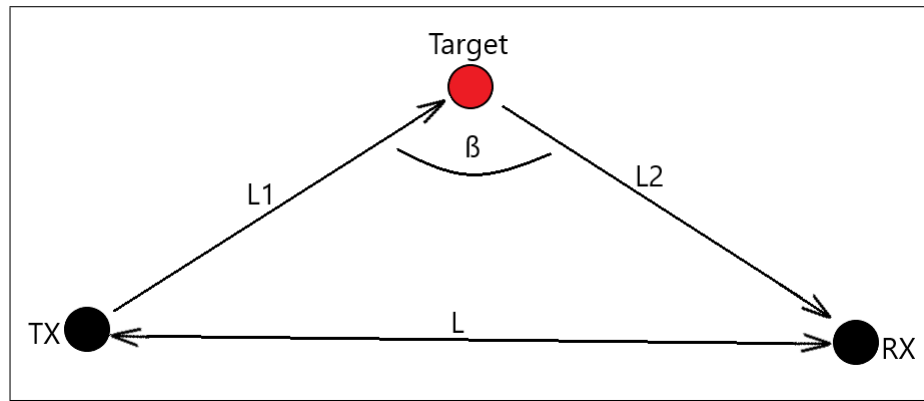
Figure 2.4: Pictorial representation of the bistatic radar system.

In Figure 2.4, the system is composed by one TX node and one RX and the distances denoted as L, L_1 and L_2 are defined in the same way as before: they represent the distances between the stations, the TX and the target and the RX and the target respectively; finally, the angle β is called the bistatic angle. Each part's main functionality corresponds to (for in depth details refer to [9]):

- The **TX node** transmits N_S pulses of duration T_{IP} during a time frame duration of T_F (this time frame is selected to ensure that the channel response in presence of a target is not changing during T_F) [13]);

- The **RX node** registers all the data received from each pulse transmitted during a single time frame.

2.3.1 Equipment

The equipment used to perform the experiment is the Time Domain PulseOn P410 device which is shown in Figure 2.5. The main features of the nodes are: precise range measurements, fused wireless data communications, configurable transmit power and easiness to integrate with other solutions.

The PulseOn P410 devices transmit coherently pulses between 3 and 5 GHz using a bandwidth of 1.4 GHz, where the pulse repetition rate is 10 MHz. These nodes have the capabilities of working as range measuring units, slow speed data link, impulse transceiver, monostatic radar, bistatic radar, multistatic or a combination of these systems [3].
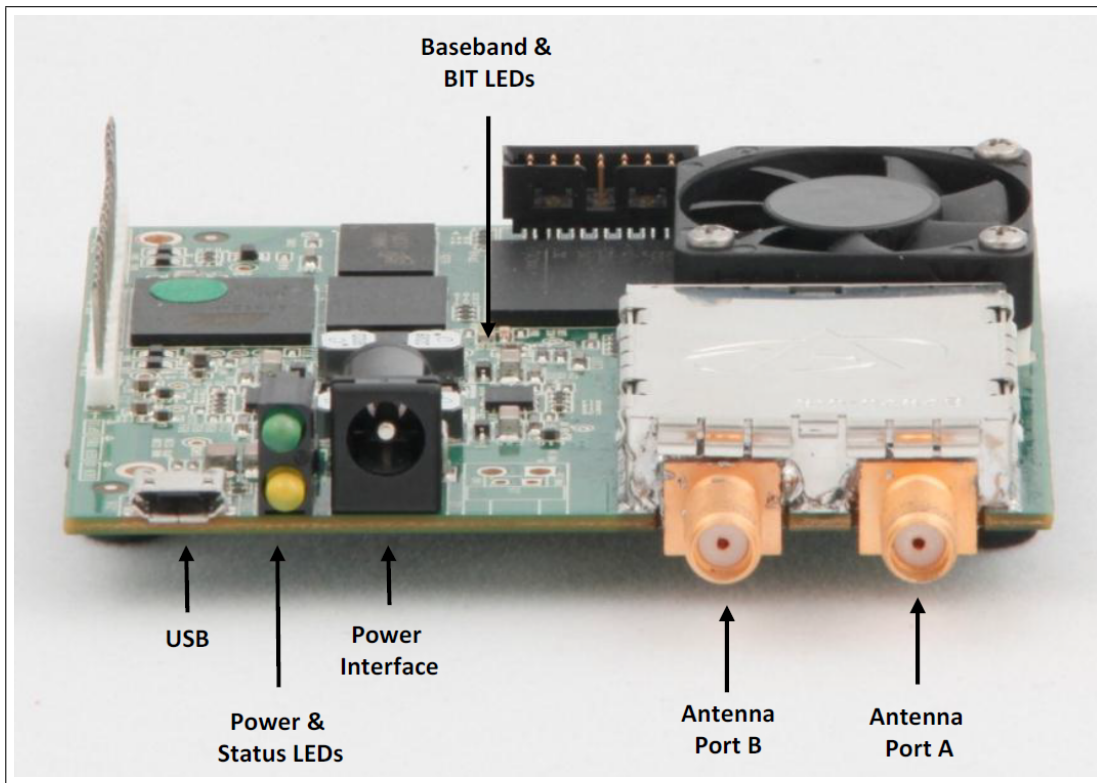
Figure 2.5: TimeDomain PulsOn 410. [2]

The hardware is configured using the RangeNet application provided by the same company, where the main parameters are set according to Table 2.1 and the parameters related to rest of the values remain in the default quantities according to the manual (see [3]).

Table 2.1: Equipment node's main parameters.

Pulse Integration Index	9
Antenna Mode	0 - Antenna A
Code Channel	3
Scan Information	0
Disable CRE Ranges	True
Transmit Gain	63 (Equivalent to 54.45 $[\mu W]$)

An important remark is that the values associated to the configuration of the RangeNet application, shown Table 2.1, are set as a temporary step to be able to properly configure the nodes in a network system. In other words, all the values set according to this table will be overwritten with the appropriate information once the following steps are performed.

After configuring the main parameters in RangeNet, the network parameters need to be

adjusted in the Configuration Tab of RangeNet/RadarNet, where the values must be set according to Table 2.2.

Table 2.2: RangeNet network parameters.

Network Mode	TDMA
NDB Update Interval	300
Max Neighbor Age	10000
NDB Size	None
Range Type	PRM
NDB Sort	ID
Range Info	All

Notice that in further steps, the TDMA network type is set to MoBi (refer to Table 2.3), this implies that the values selected for the range type and information will be deactivated and will not affect the experiments that use this configuration. Even thought, this RangeNet network temporal state is required to be able to set the TDMA network parameters.

With the configuration set to form a TDMA network, the system is prepared to properly establish the mapping table of the devices in the network. Once the network main parameters are selected, the specific values in the *TDMA tab* are set to a configuration of two devices (one working as transmitter and another one as receiver) using the values according to Table 2.3.

Table 2.3: TDMA network parameters.

Requester ID	100
Responder ID	102
Integration Index	5
Channel Code	0
Antenna Mode	0 - Antenna A
Req. Data	Not Selected
Rsp. Data	Not Selected
Type	MoBi
TX Scan Idx	2
RX Scan Idx	2
Sleep	Not Selected
Manual Time	100.000

Once the TDMA values are properly set, it is required to ensure that the slot map is properly configured by pressing the buttons *Get* and *Set* in the slot map functionality.

From Table 2.3, the device whose identification number is 100 works as the transmitter and the node 102 as the receiver and now, it is convenient to remember that, for the purposes of this work, only a bistatic radar configuration is required (refer to Section 2.1 for details).

By setting the *Integration Index* to 5, the PulseOn P410 devices perform an averaging operation over 2^5 acquired signal. In other words, before reporting the waveforms to the user, the equipment transmits and acquires at least 2^5 sets of pulses, with the 2^5 waves received, an averaging operation is performed and the result of this computation is then reported in the user's application.

With the parameters *Req. Data*, *Rsp. Data* and *Type* set to the values indicated in Table 2.3, all the ranging report functionality of the equipment is deactivated.

The functionality used in the RangeNet application to obtain the experiment data is the **Logging Tab**. With this tool, all the node's received messages (including protocol overhead and scan's data) are recorded into a *csv* file. These *csv* files are processed by the Matlab code (refer to Section 2.4) and finally produce the received power scattered by the target under study which allows to calculate the path loss exponent.

2.3.2 Target Determination

Prior to start the experiment, it was required to determine the most convenient shape of the object to use as a target. After a bibliographic review was performed, the target shape selected was the sphere.

An advantage related to the spherical shape of a target is that the position of the object with respect to the TX and RX stations, does not change its RCS. This implies that it is not required that the target is set in a specific position, to have the term σ in (2.1) as constant as possible during the experiments. Also, since the position of the target is set by the experiment's operator, by having a target shape invariant in all axis, it is possible to remove the influence related to the human error when collocating the target.

Another advantage of selecting a sphere is that the creeping and specular waves produced by its shape can be associated to the geometry of the object and estimated accordingly [7]. Since the present work's goal is to account for all the target's scattered power, it is required to calculate the shortest path (specular) and the longest path (creeping route # 2 in Figure 2.6) and once these routes are estimated, properly apply them to the received signal at the RX.

If a two dimensional analysis of the sphere is carried out, the specular trajectory of the electromagnetic wave produces the first echo peak received (shortest path associated to the smallest ToA), while the last peak received (longest path related to the largest ToA) is due to the creeping wave 2 as indicated in Figure 2.6.
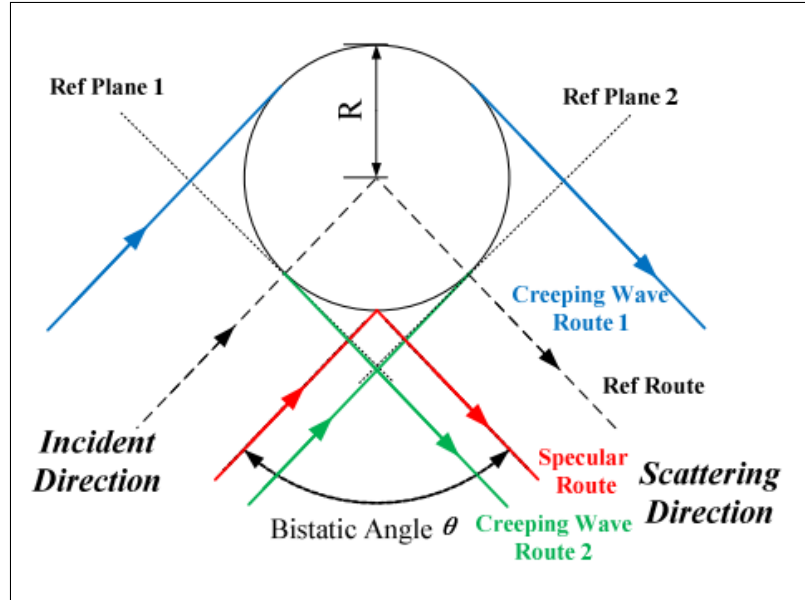
Figure 2.6: Specular and creeping paths over a sphere [7]

Using the previous analysis, if the stations' and target's locations are known, it is possible to calculate the geometrical parameters required to determine the values of L_1 and L_2 associated to the specular and creeping directions, which means that it is possible to accurately estimate the time window in which the scattered signal from the sphere is received in the RX node. In fact, this computations are required to determine the path loss exponent α. In general, the required equations are:

$$t_{min} = \frac{L_1^{specular} + L_2^{specular} - L}{c} \tag{2.3}$$

$$t_{max} = \frac{L_1^{creeping\#2} + L_2^{creeping\#2} - L}{c} \tag{2.4}$$

where the variables L_1 and L_2 refer to the distance between the TX and RX to the target's positions as depicted in Figure 2.6, L refers to the baseline distance and c to the speed of light. While t_{min} and t_{max} are the boundaries in the time domain that define the window.

2.4   Data Processing Code

To process the raw data collected by the RX node, code based on the algorithm described in [14] was used. In this particular case, the code pipeline corresponds to:

1. Load the empty room (ER) scan data received by the RX node;

2. Align 20 ER scan data among each other;

3. Calculate the mean of the 20 received ER scans [1] (this will contribute to reduce the influence of Gaussian noise even further);

4. Read 20 scan wave-forms from the data file corresponding to a static position of the target;

5. Align the target's scan data with each other;

6. Calculate the mean of all the scan wave-forms just aligned;

7. Repeat from step 4 for all the target positions in a single experimental scenario;

8. An envelop filter as described in [14] is applied to the ER and scan data;

9. The targets' scan data and the ER information is aligned to a suitable leading edge (at 20 ns);

10. The scan data clutter is removed by subtracting from the target's wave-forms the ER wave-form.

After the modified clutter removal code is executed, additional processing is required to compute the desired received power from the sphere scattering. This code's functionality corresponds to:

1. Calculate the time window for each point in the experiment;

2. Extract from the clutter-free wave the section according to the time window;

3. Calculate the energy and power related to the time window;

4. Store in the file *Energy Power Data.csv* all the calculated information related to L, L_1, L_2, $Energy$ and $Power$ for each target position in the experiment.

---

[1]The Matlab code calculates the average of 20 waveforms logged using the RangeNet application, but these logged waveforms are the result of averaging $2^{Integration\ Index}$ signals. The process prior to the logging step is performed by the equipment itself and it is important to remember that the Integration Index used in this experiment is set according to the value in Table 2.3.

The code was developed in the Matlab environment and the resulting output is the curve of received scattered power from the sphere P_r^{target} as function of $10\alpha \log_{10}(L_1 L_2)$.

As an important specification, to be able to process the data, the code required the files to be organized in the following manner:
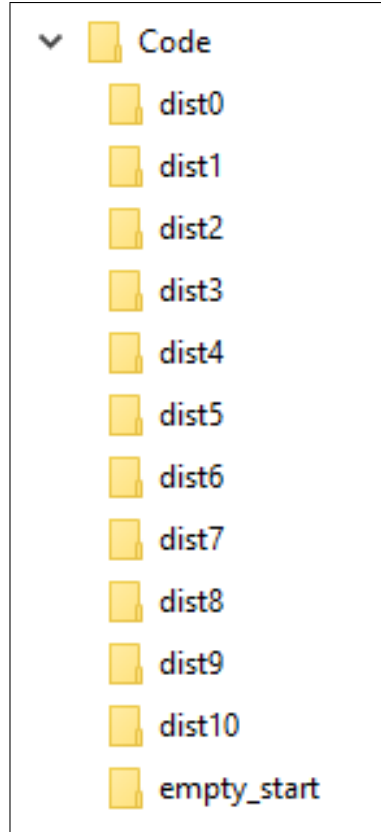
Figure 2.7: Code folders' hierarchy.

The folders shown in Figure 2.7 are:

- **empty_start:** contains all the *empty room* measurements enumerated as: "1.csv", "2.csv", "3.csv"... Where each number identifies *individually* each oval;

- **dist0:** has the data of the *first points* of each oval. In this folder, the files are named with the same methodology: "1.csv", "2.csv", "3.csv"... where each number identifies individual ovals;

- **Rest of distX:** these folders store the files for the *second, third, fourth... points* of each oval. The naming convention is the same as dist0.

In other words, to process the data, first take the files corresponding to one Cassini oval,

move the one containing the empty room information to the folder "empty_start" and rename it as "1.csv". Then, move the file with the measurements of the first point to "dist0" and change the name to "1.csv". After this, take the data from the second point and move it to folder "dist1", once again rename this file as "1.csv". Keep this procedure until all the files have been reorganized in the "distX" binder.

Proceed in the same way as described in the previous paragraph with the next Cassini oval, but for this set of data, name the files as "2.csv". Continue organizing all the files collected until this hierarchy is met.

With all the *csv* in the correct place, move the code in charge of processing the files to the folder "/Code/". In this case, the files to include are: AutomatedRun.m, EnvelopeFilter.m, MainPower.m, ReadCSV.m, SaveCSV.m, SNR_AlignmentLED.m, WindowER_AlignmentLED.m and Taps_EnvelopeFilter.csv.

Finally, to execute the code, set the parameters in AutomatedRun.m according to the experiment and run the script. Once the data is processed, the output files are created inside the folder "/Code/". Additionally, to produce the graphs used in the present work, the script MainDataAnalysis.m is used.

Chapter 3

First Experiment: Laboratory of Electronics and Telecommunications

3.1   Room Description and Preparation

The first experiment was developed in the LEle of the DEI "Guglielmo Marconi" of the University of Bologna with location in Cesena. The room has an area of 14 m by 10.5 m in which there are distributed tables and electrical equipment, as can be seeing in Figure 3.1.

Figure 3.1: Photograph of the LEle laboratory.

First, as a preparation for the measurements, the room was marked to indicate the locations

of: the RX device, the TX station and several positions in six different Cassini ovals. All of these spots were selected accordingly to the room objects and their distribution is presented in Figure 3.2
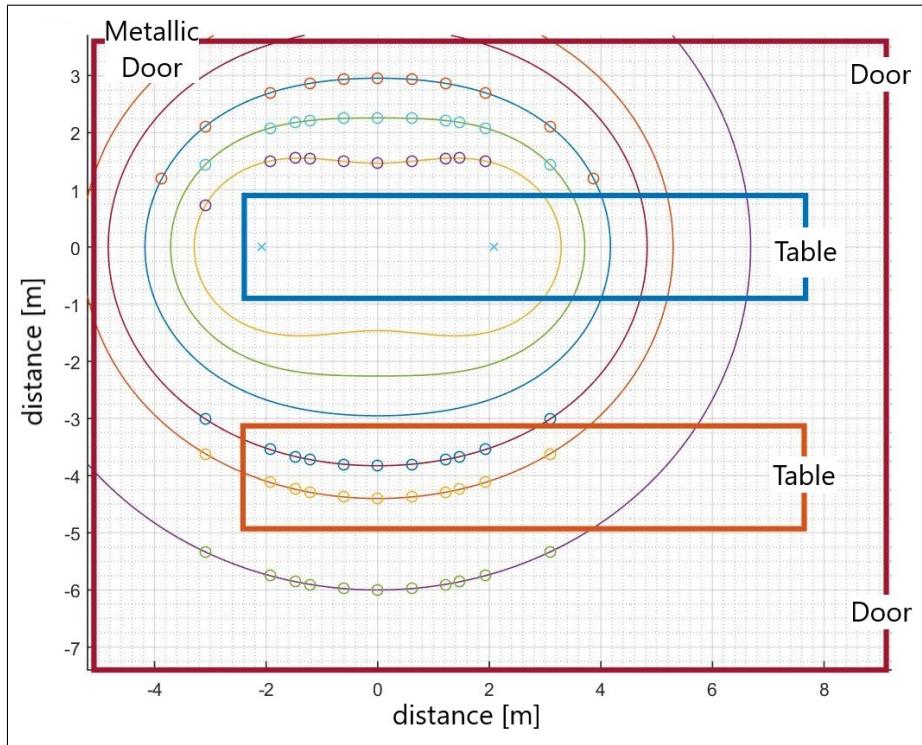
Figure 3.2: Diagram of the locations of interest in the LEle laboratory.

Once the required points were set, the following procedure was followed to collect the data:

1. The TX and RX nodes were installed according to Figure 3.2 in the coordinates (-2.0825,0) and (2.0825,0) respectively;

2. With the room empty, the received wave-forms were logged using the RangeNet application;

3. The selected object for testing (target) was set in one of the positions shown in Figure 3.2 -in this case, as discussed in Section 2.3.2, the testing subject is a metallic sphere- then, the operator left the test's area and recorded the received wave-forms;

4. The step 3 was repeated for all the points selected in a single Cassini oval;

5. With all the measurements performed for a single oval, steps 2 and 3 were repeated until all the data were collected.

3.2   Data Processing

With all the data saved, the files and the code need to be arranged in the specific hierarchy as described in Section 2.4. Once the arrangements were performed, the code was used to produce the results presented in this chapter.

As a first intermediate step of the algorithm, the results of averaging the 20 wave-forms acquired for the ER is shown in Figure 3.3
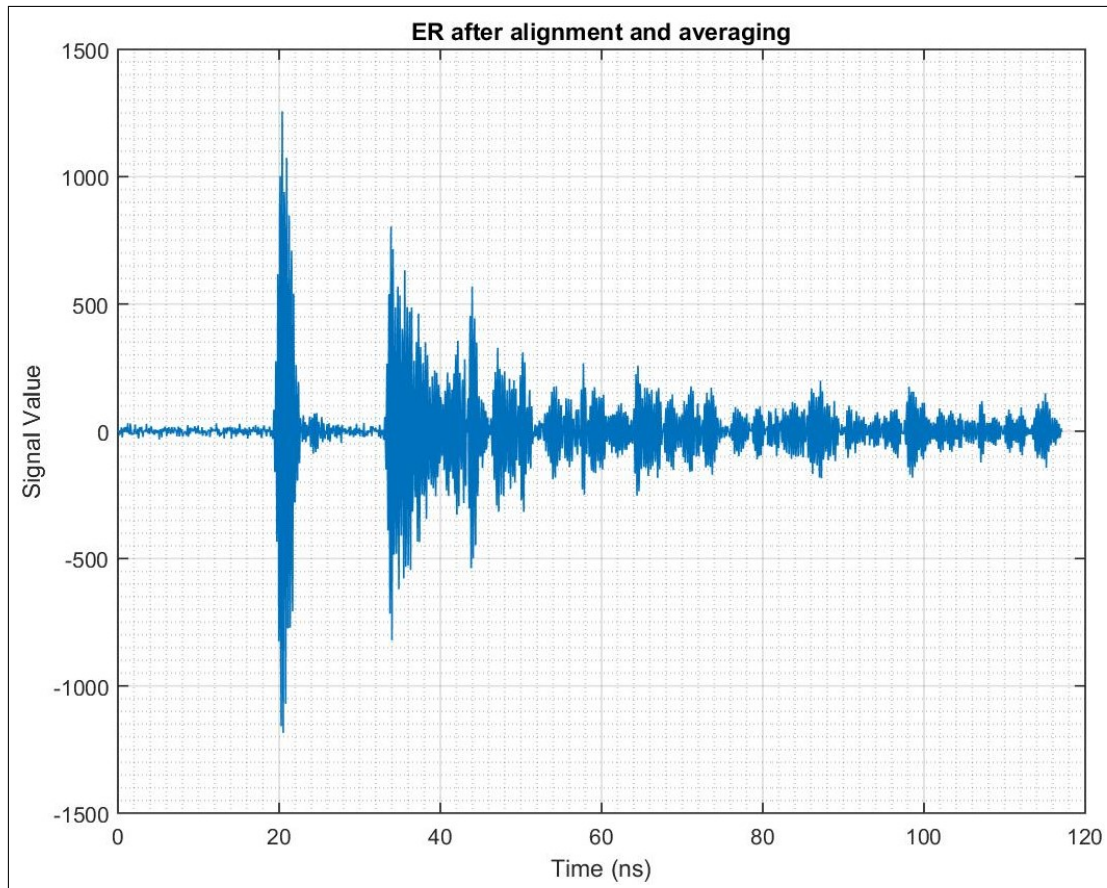
Figure 3.3: Empty Room signal after alignment and averaging.

From the figure with the ER after averaging, it can be seeing that noise corrupting the measurement is almost negligible due to the difference in their amplitude values: the signal's level prior to the leading edge arrival is around 25 while the leading edge peak is close to 1250.

It is important to remember that the Pulse 410 equipment used during this experiment performs a previous integration step, and this step is configured using the parameter *Integration Index*. As shown in Table 2.3, this value was set to 5 for the current work which means that the radio acquires 2^5 wave-forms, calculates the average of all this information and finally, logs the resulting signal. Then, from this logged data, 20 signals are input into the algorithm to calculate

the average reported in Figure 3.3.

With the ER signal ready, the same procedure is performed for the data collected at all points in the oval. In Figure 3.4, the first measured point from the third oval of the LEle laboratory is presented.
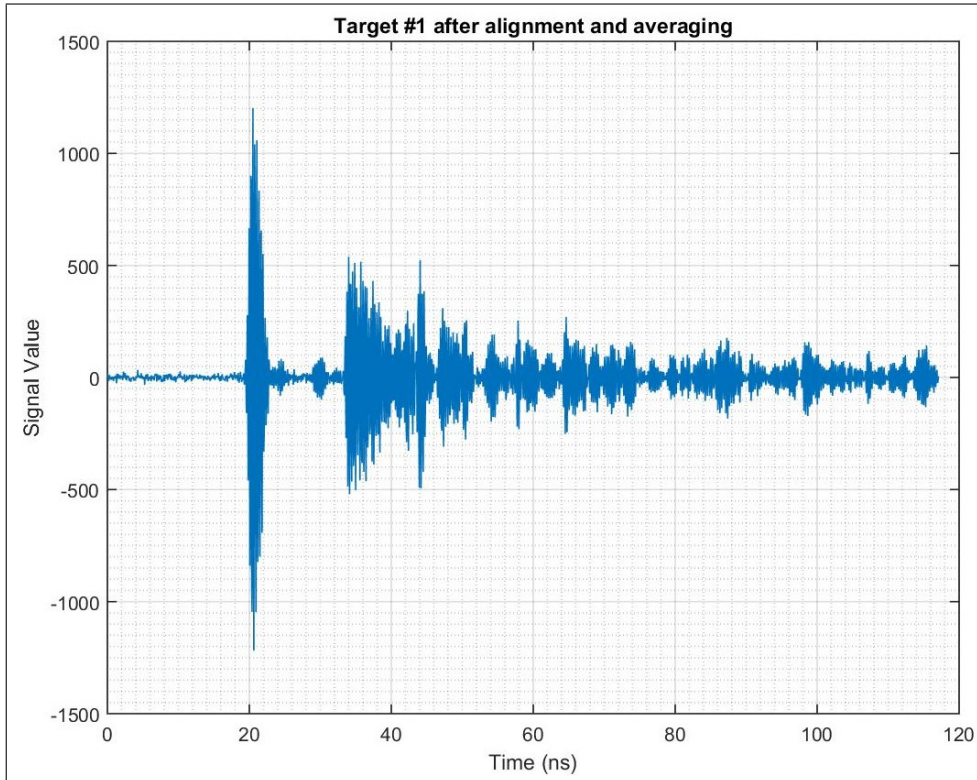
Figure 3.4: Processed waveform of the target 1 in the third oval of LEle laboratory.

As expected, the result of aligning and averaging the 20 wave-forms of the target's data is similar to the ER result. In this case, the main feature of this procedure is that the SNR is highly increased in the same manner for both signals.

Ideally, in Figure 3.4 all the information presented should be only due to the ER and the target's contributions, therefore when the ER signal is subtracted the remaining wave should be only related to the target's scattered signal but as it will be analyzed later, there will be additional peaks after this operation (these peaks are called "residual clutter"). This phenomena will be discussed later in this thesis once the clutter removal algorithm is finished and a cleaner waveform is obtained.

With the averaged signals calculated for all the target's points around a single Cassini oval, the next step is to extract the envelop from the wave-forms. Figure 3.5 and Figure 3.6 illustrate the result of this step for the empty room and the same target's position as previously discussed.
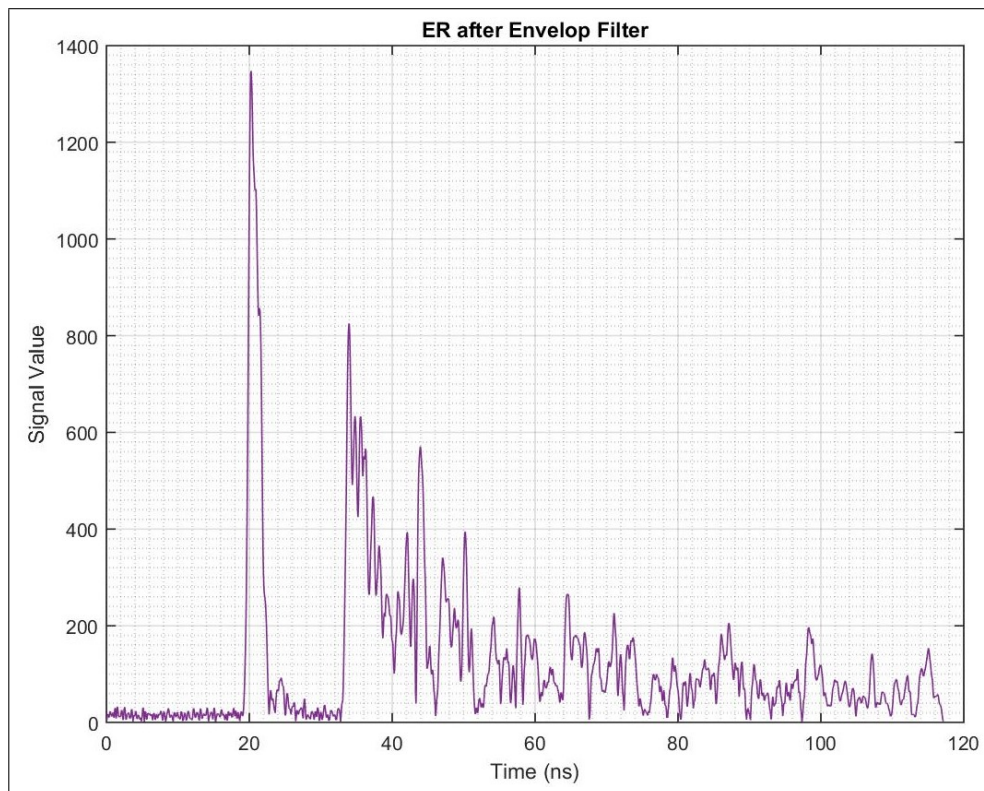
Figure 3.5: Empty Room signal after envelop extraction.
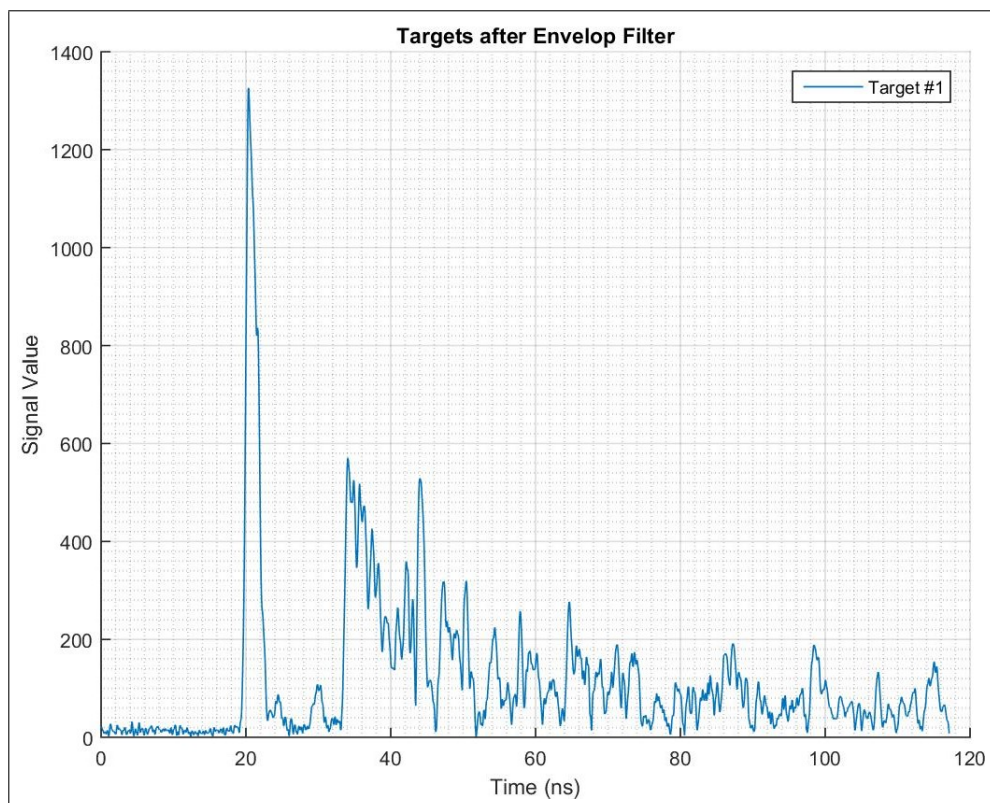
Figure 3.6: Target 1 signal after envelop extraction.

With both envelop filtered signals, the following step is to calculate the difference between them. The resulting signal is presented in Figure 3.7.
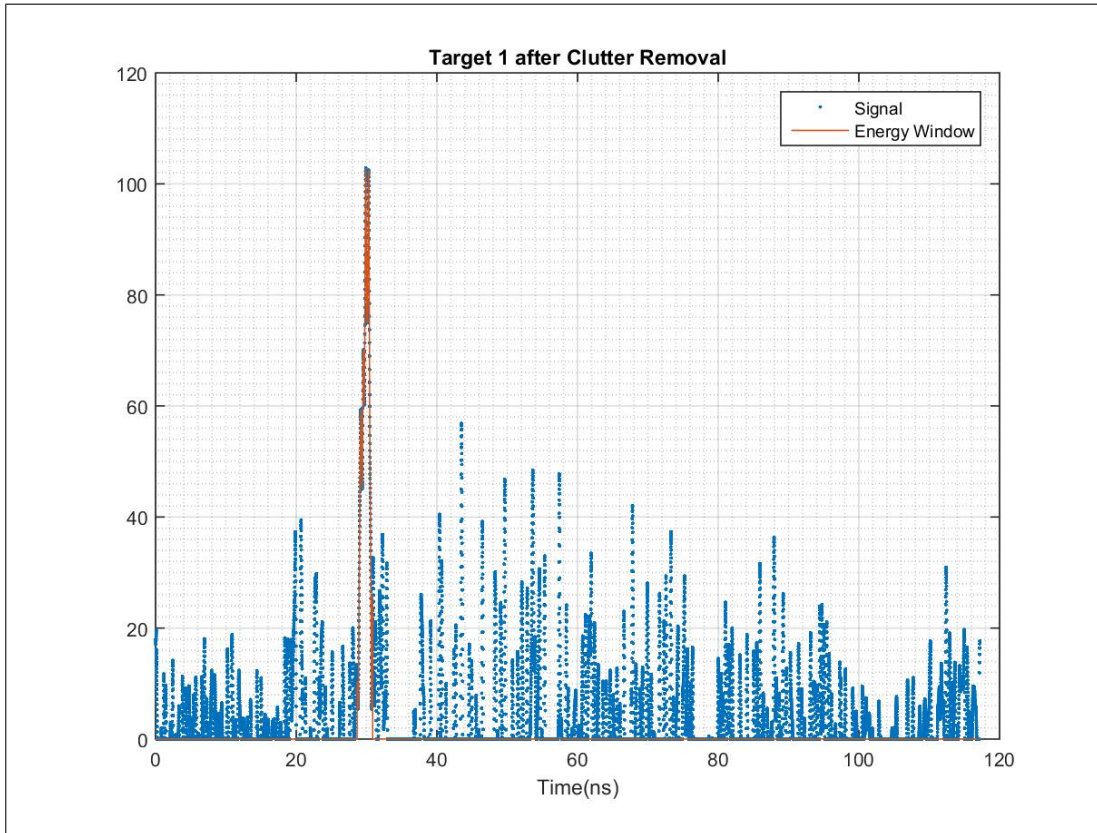
Figure 3.7: Target 1 clutter free signal.

The waveform in Figure 3.7, in the ideal case, includes the data only due to the influence of the target (signal scattered by the object). However, as it can be seeing from the obtained result, other factors affected the output (noise and imperfectly removed clutter), this is appreciated since there are additional peaks along the entire time domain. Even though several peaks are presented in the *"clutter free"* signal, with the aid of a time window calculated according to the target's position, it is possible to isolate the signal due to the scattering of the object of interest.

For the specific case of the third oval in Figure 3.2, the corresponding target's points are listed in Table A.3. Using these coordinates in conjunction with the dimensions of the target and geometric rules as depicted in Figure 2.6, it is possible to calculate the time window as described in Section 2.3.2.

Once the time window is fixed in the signal after clutter removal, the scattered power from the target is calculated using (2.2). For the sake of completeness of the present example, the resulting power for the first point in the third Cassini oval inside the LEle Laboratory is 35.7471 dB.

If the *"clutter free signals"* are analyzed manually, one can notice different behaviors in some results, in other words, the waveform presented in Figure 3.7 is just one particular form in which it is evident where is the target and the remaining wave peaks (the residual clutter) have significantly lower magnitudes than the main peak's (the target). Some of this differences are presented in Figures 3.8 and 3.9.
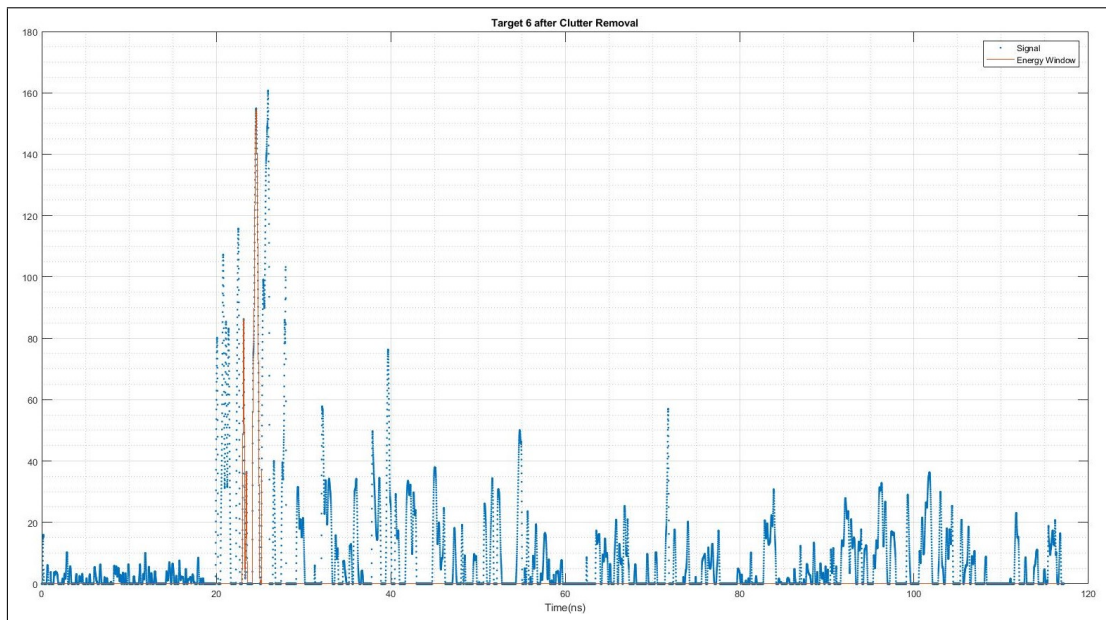
Figure 3.8: Target 6 clutter free signal from first oval in LEle.
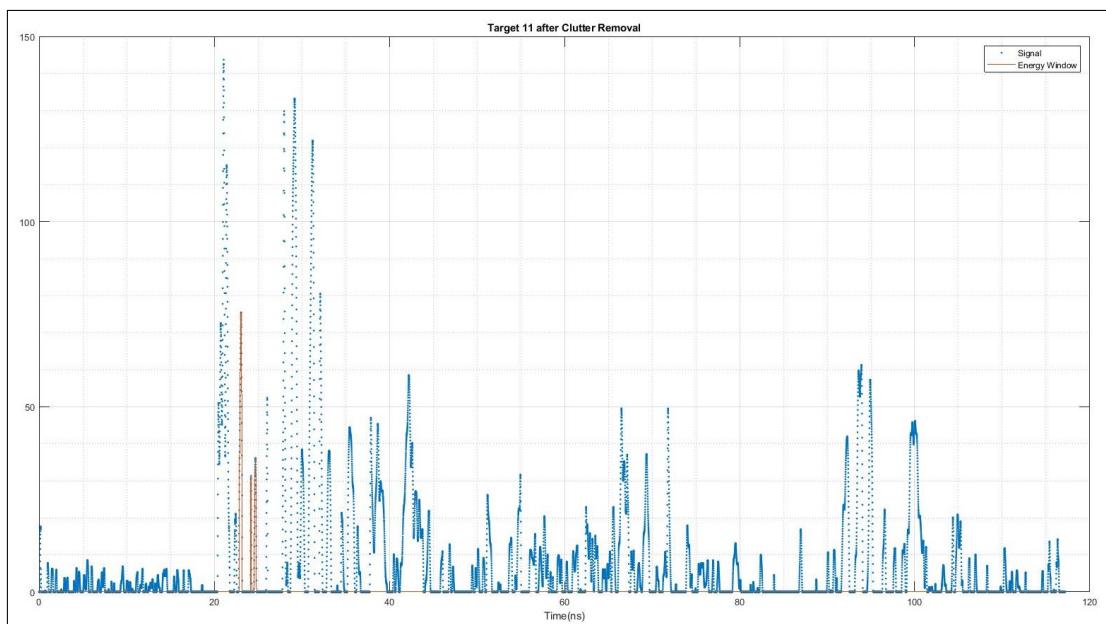
Figure 3.9: Target 11 clutter free signal from first oval in LEle.

The signals in Figure 3.8 and Figure 3.9 show how difficult target detection could be even after the clutter removal algorithm. These cases occur due to the fact that several objects in the

room might have combinations of $L_1 \cdot L_2$ comparable to the target's value; this means that the time window will not only contain the target's scattering power but also additional contributions from the room objects.

In Figure 3.8 it can be appreciated that the clutter coming from objects (with similar distance as the target's) contributes possibly in a constructive form as there are several peaks of comparable magnitudes inside and near to the time-window's boundaries. In the other hand in Figure 3.9, it can be seen how the influence of objects (remember similar values of $L_1 \cdot L_2$ as the target's) possibly affected the received wave-form in a destructive way since the peaks inside the time-window are smaller than the others in the vicinity.

The cases presented in Figures 3.8 and 3.9 reveal that there is a limitation on the experiment methodology since there is no deterministic technique to ensure that the scattered power inside the time-window is due to the target and only itself. However, this method is accurate enough for this document particular interests: calculate the path loss exponent.

3.3   Path Loss Experimental Curve

The process previously described was repeated for all the points in each Cassini oval and since the Cartesian coordinates for each point are known, the graph of power in function of distance can be built as Figure 3.10 outlines.
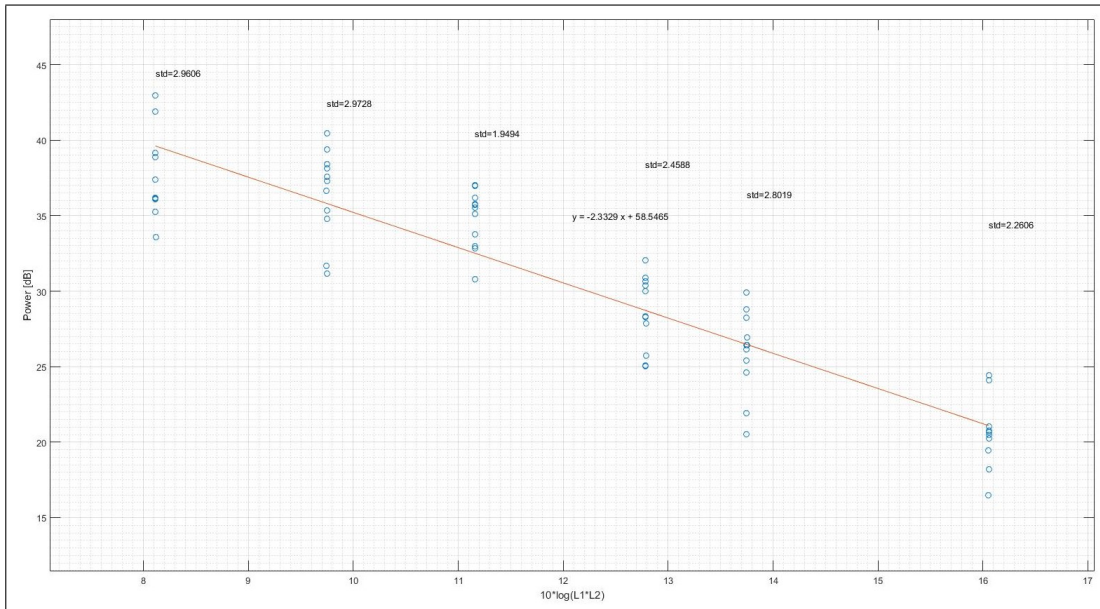
Figure 3.10: Power vs $10 \log_{10}\left(L_1 L_2\right)$ for the LEle laboratory.

The data in Figure 3.10 have an average standard deviation of 2.5673 and the least-square

fitting curve is given by $P[dB] = -2.3329 \cdot \left(10 \log_{10} \left(L_1 L_2\right)\right) + 58.5465$. This equation indicates that the **experimental path loss exponent calculated for the LEle laboratory is 2.3329**.

The obtained value for the LEle laboratory meets the expectations for the experiment. In fact, a comparison with the theoretical path loss exponent of free space, that is 2, reflects how the influence of a cluttered indoor environment increases the value of α, which means that the received power decays 16.6 % faster in this specific indoor environment than in free space due to $\alpha_{LEle} > \alpha_{free\ space}$.

3.4   Residual Clutter Statistics

As an addition to the present work, once the *path loss exponent* of the LEle laboratory was determined, the statistics of the residual clutter were computed and the basics for a mathematical model were proposed.

To produce the histogram (discretized probability density function) of the residual clutter, all the target's contribution was removed from the output signal of the clutter removal algorithm. As an example to clarify this procedure, consider the wave in Figure 3.7. In this signal, all the information inside the time window was removed and saved, this procedure was repeated for all points in the experiment and once all the residual clutter vectors were saved, they were concatenated and used to calculate the histogram depicted in Figure 3.11.
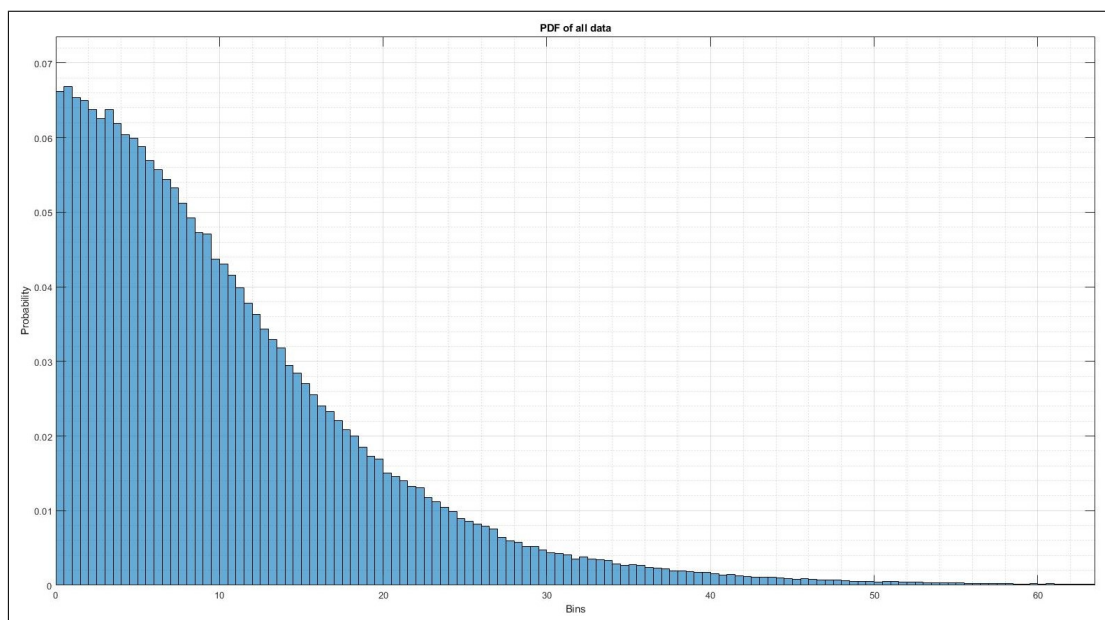
Figure 3.11: Histogram of LEle laboratory residual clutter.

The calculated mean and variance for the residual clutter data were 10.7847 and 96.9978 respectively. Finally, a proposal for the residual clutter probability density function was set as:

$$f_R(r) = \mathbb{P}(R = 0) \cdot \delta(r) + [1 - \mathbb{P}(R = 0)] \cdot g_R(r) \tag{3.1}$$

where δ is the Dirac impulse.

The model presented in (3.1) is composed by two main terms:

- $\mathbb{P}(R = 0) \cdot \delta(r)$: this term is related to the zero values in the residual clutter signal (when $R = 0$). Zero values are originated by two causes: (1) the algorithm effectively removed all the contribution of the clutter in a specific time window; (2) the rectifier used after the envelop extraction introduced them when removing the negative values.

- $[1 - \mathbb{P}(R = 0)] \cdot g_R(r)$: this term is related to obtained histogram from the residual clutter of the LEle laboratory. In this term, the function $g_R(r)$ needs to be properly estimated to follow the experimental data presented in Figure 3.11.

In principle, the estimation of the terms $\mathbb{P}(R = 0)$ and $g_R(r)$ is possible and can be computed using different approaches. However this task is out of the scope of the present work and will be remitted to future endeavors.

Chapter 4

Second Experiment: "DEI Department's Garage"

4.1 Room Description and Preparation

As a second experiment, it was selected the garage of the DEI of the University of Bologna at Cesena. This basement is a large area containing some spare equipment, furniture and the parking spaces for several cars. A photography of the room is shown in Figure 4.1.
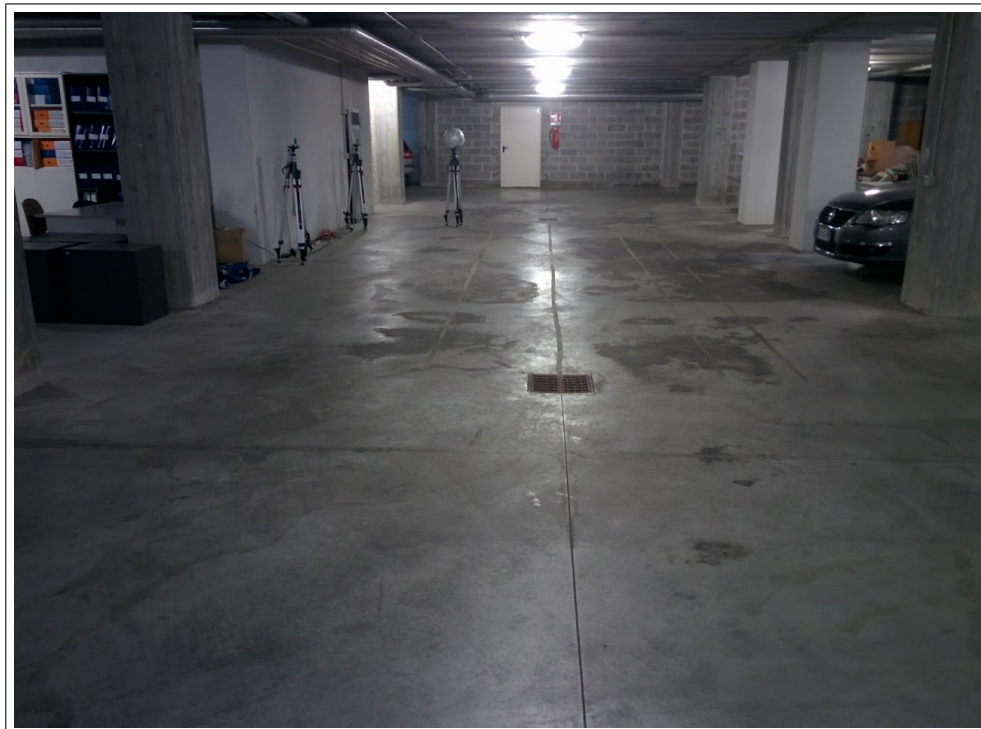
Figure 4.1: Photography of DEI's garage.

Once again, six Cassini ovals were marked in the experimental area. Each of these ovals had eleven points and all of this points were evaluated using the same target as described in Chapter 3. The coordinates of each position are presented in Figure 4.2 and they are enlisted in Appendix A.2
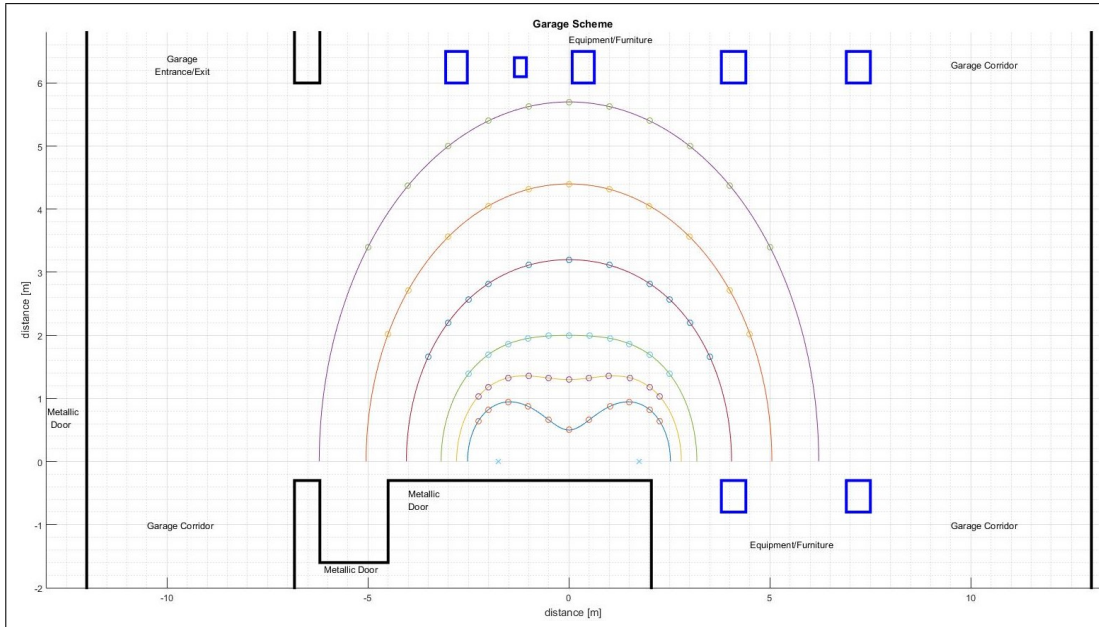
Figure 4.2: Diagram of locations of interest in the DEI's garage.

In the same manner as the LEle laboratory, the garage required the step preparations as:

1. The TX node was installed in the coordinates (-1.75,0) while the RX was set in (1.75,0);

2. The ER information was logged using the RangeNet application;

3. The target (metallic sphere) was collocated in one of the selected positions specified in the diagram of Figure 4.2, then the wave-form data was recorded;

4. The step 3 was repeated for all points in a single oval;

5. Finally, the ER and targets' data acquisition was recorded for all ovals.

4.2   Data Processing

The processing chain used to produce the results of the DEI's Garage is the same as the one described in Section 3.2, therefore we refer the reader to the previous explanation for in depth details. If an example case for the garage is desired, the intermediate steps of the point

#4 from the first oval (smallest) as indicated in Figure 4.2 and Table A.7 are included in Annex B.

4.3 Path Loss Experimental Curve

In this particular case, with all the information collected and processed, once again, the graph of the target-scattered power as a function of $10\log_{10}\left(L_1 L_2\right)$ is built as presented in Figure 4.3.
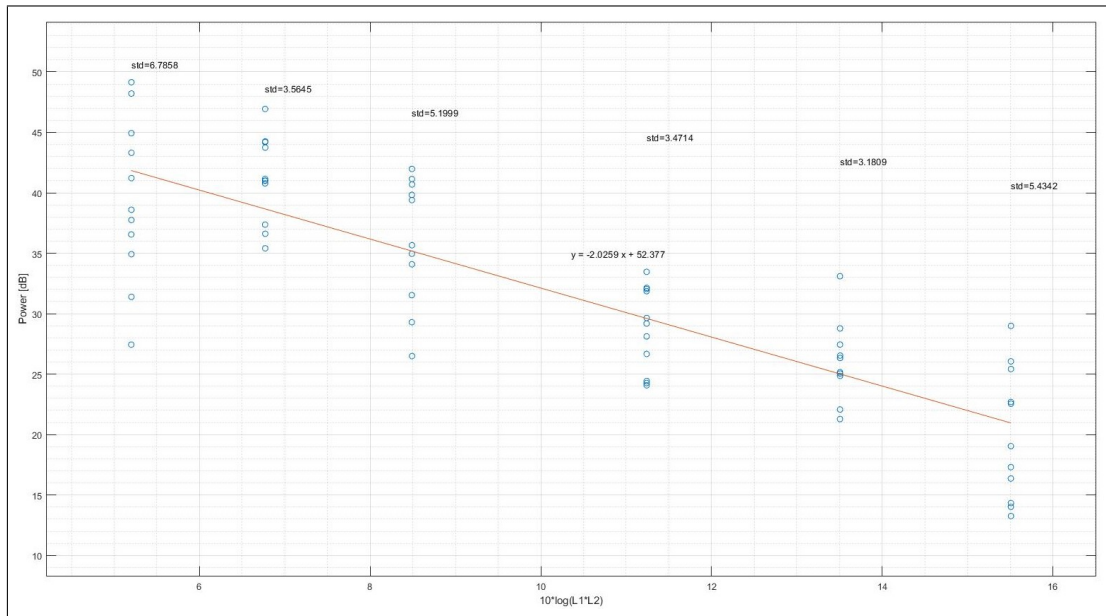
Figure 4.3: Power vs $10\log_{10}\left(L_1 L_2\right)$ for DEI's Garage.

In the previous graph, the average standard deviation of the data is 4.6061. The least-square curve equation is given by: $P[\text{db}]= -2.0259 \cdot \left(10\log_{10}\left(L_1 L_2\right)\right) + 52.377$ which means that the estimated experimental **path loss exponent of the DEI's Garage is 2.0259**. If this value is compared with the free space parameter we see that $\alpha_{DEI\ Garage} > \alpha_{free\ space}$, in particular the received power decreases in a 1.3% faster in this specific indoor environment than the free space.

The path loss exponent of the DEI's Garage (2.0259) is closer to the free space value than the LEle laboratory's result (2.3329). This is due to the fact that the Garage is a less cluttered environment than the LEle laboratory: it is possible to corroborate this condition (even by simple sight) when the pictures in Figures 3.1 and 4.1 are analyzed. Additionally, these values of path loss exponent reaffirm that the experimental results obtained with the present methodology followed the expected tendency.

4.4   Residual Clutter Statistics

Additionally, as it was done for the LEle laboratory, the statistics of the residual clutter of the DEI's Garage were computed.

In this case, the residual clutter information was recorded directly using the RangeNet application. To calculate the histogram (probability density function), 1002 empty room waveforms were recorded in the garage: two of these scans were selected as the *"ER"* information and then, the code was used to apply the clutter removal algorithm to all the remaining 1000 vectors. Once all the residual clutter was computed, these waves were concatenated and Figure 4.4 was produced.
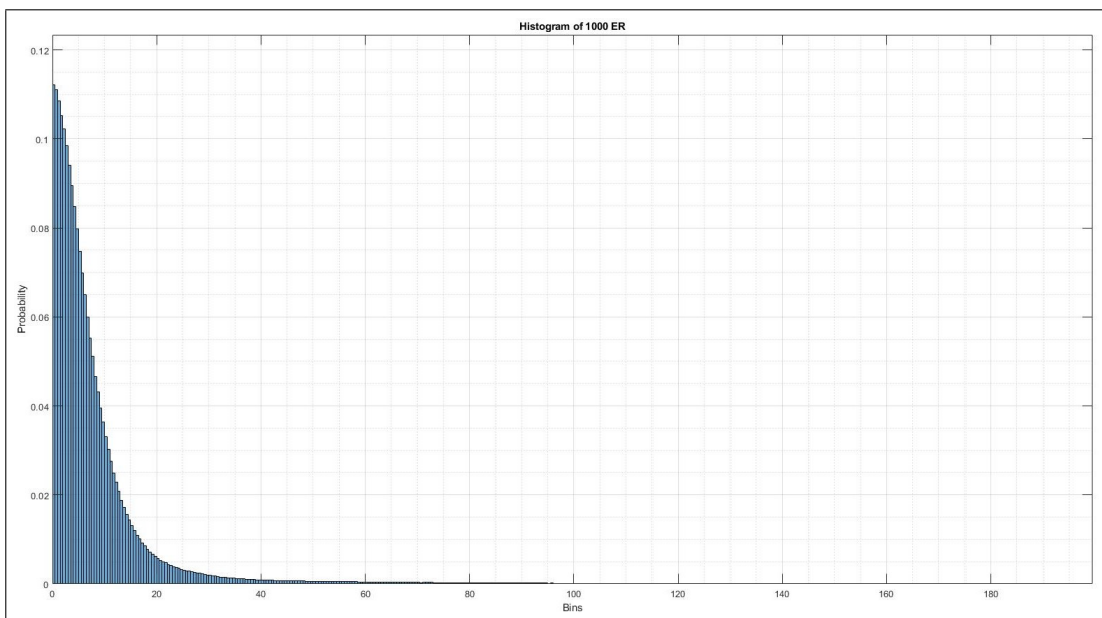
Figure 4.4: Histogram of DEI's Garage residual clutter.

The proposed probability model for the DEI's Garage is the same as the one suggested for the LEle Laboratory (c.f. (3.1)). Importantly, the environment specific quantities $\mathbb{P}(R = 0)$ and $g_R(r)$ need to be computed and this task is deferred to future work.

Chapter 5

Conclusion and Recommendations

5.1 Conclusion

The code functions used to calculate the Cassini ovals produced a satisfactory output, allowing the operator to obtain points according to the needs of the indoor room and therefore, enhancing the preparation of facilities by marking the desired target's positions in an accurate manner.

The implementation of the specular and creeping wave routes technique that relates the geometry of a spherical target to these quantities, allowed to estimated with high accuracy the echoes of the object of interest among all the data received by the equipment.

The Matlab code developed allowed to calculate the power received from the scattered signal associated to the spherical target in a accurate manner. This means that using the current methodology it was possible to compute the entire plot of energy as a function of the distance and therefore determine the path loss exponent for indoor facilities as: 2.3329 (LEle) and 2.0259 (Garage).

The methodology presented in this work permitted to obtain properly the data related to the "residual clutter" that is characteristic of the LEle laboratory and the DEI's Garage, this information was properly processed and the corresponding histograms were elaborated. Finally, these graphs are required to calculate the mathematical model that is deferred to future works.

5.2   Recommendations

To perform the current experiments, a metallic tripod was used to fix the target in most of the given positions. However for some locations in the LEle laboratory it was not possible due to the furniture inside the room. This causes the RCS of the target to vary along the experiment, which causes the function $g(f, f_L, B)$ in (2.1) to be variable. Avoiding this problem could increase the fidelity of the measurements even though, this could imply a troublesome endeavor.

A suitable mathematical expression is required to be used as an input to estimate the probability model from the histograms of the LEle Laboratory and DEI's Garage. To determined this expression it would be advisable to perform a bibliographic review related to fitting models and the available software to obtain satisfactory results that follow the entire histograms.

Bibliography

[1] M. Chiani, A. Giorgetti, and E. Paolini. Sensor Radar for Object Tracking. *Proceedings of the IEEE, submitted*.

[2] Time Domain. Quick Start Guide PulsOn 410 RCM Development Kit, 2012. URL http://www.timedomain.com/.

[3] Time Domain. RangeNet Reconfiguration and Evaluation Tool (RangeNet RET) User Guide, 2013. URL http://www.timedomain.com/.

[4] B. Gulmezoglu. Indoor multi-person tracking via ultra-wideband radars. Ph.D. dissertation, Bilkent University, 2014.

[5] B. Gulmezoglu, M. B. Guldogan, and S. Gezici. Multiperson tracking with a network of ultrawideband radar sensors based on Gaussian mixture PHD filters. *IEEE Sensors J.*, 15(4), Apr. 2015.

[6] M.C. Jackson. The geometry of bistatic radar systems. *IEE Proceedings F*, 133(7), Dec. 1986.

[7] M. Lyu, Y. Zhang, Y. Wu, and G. Li. Research on the bistatic scattering characteristics of metal sphere. *IEEE Internation Conference on Automated and Trusted Computing*, 2015.

[8] A. V. Oppenheim, R. W. Schafer, and J. R. Buck. *Discrete-Time Signal Processing*. Prentice-Hall Signal Processing Series. Prentice Hall, 2nd ed edition, 1999.

[9] E. Paolini, A. Giorgetti, M. Chiani, R. Minutolo, and M. Montanari. Localization Capability of Cooperative Anti-Intruder Radar Systems. *EURASIP Journal on Advances in Signal Processing*, 2008.

[10] B. Sobhani, M. Mazzotti, E. Paolini, A. Giorgetti, and M. Chiani. Effect of state space partitioning on bayesian tracking for UWB radar sensor networks. *IEEE International Conference on Ultra-Wideband*, Sep. 2013.

[11] B. Sobhani, M. Mazzotti, E. Paolini, A. Giorgetti, and M. Chiani. Multiple target detection and localization in UWB multistatic radars. *IEEE International Conference on Ultra-Wideband*, Sep. 2014.

[12] B. Sobhani, E. Paolini, A. Giorgetti, M. Mazzotti, and M. Chiani. Bayesian tracking in UWB radar sensor networks. *IEEE International Conference on Communications, Workshop on Advances in Network Localization and Navigation*, Jun. 2013.

[13] B. Sobhani, E. Paolini, A. Giorgetti, M. Mazzotti, and M. Chiani. Target Tracking for UWB Multistatic Randar Sensor Networks. *IEEE Journal of Selected Topics in Signal Processing*, 8:125–136, Feb. 2014.

[14] F. Valmori. UWB Radar Sensor Networks: Detection Algorithms Design and Experimental Analysis. Master's Degree in Electronics and Telecommunications Engineering for Energy, School of Engineering and Architecture, University of Bologna, 2014.

[15] F. Valmori, A. Giorgetti, M. Mazzotti, E. Paolini, and M. Chiani. Indoor Detection and Tracking of Human Targets with UWB Radar Sensor Networks. *IEEE International Conference on Ubiquitus Wireless Broadband*, Oct. 2016.

Appendix A

Cassini Ovals' coordinates

A.1   LEle laboratory

In this section, all the Cartesian coordinates of the measured points in the LEle laboratory are presented.

Table A.1: First oval's points in LEle laboratory.

Point	X coordinate	Y coordinate
1	0	1.463
2	0.61	1.5
3	1.215	1.552
4	1.47	1.554
5	1.931	1.504
6	3.089	0.7268
7	-0.61	1.5
8	-1.215	1.552
9	-1.47	1.554
10	-1.931	1.504
11	-3.089	0.7268

Table A.2: Second oval's points in LEle laboratory.

Point	X coordinate	Y coordinate
1	0	2.258
2	0.61	2.25
3	1.215	2.212
4	1.47	2.18
5	1.931	2.081
6	3.089	1.441
7	-0.61	2.25
8	-1.215	2.212
9	-1.47	2.18
10	-1.931	2.081
11	-3.089	1.441

Table A.3: Third oval's points in LEle laboratory.

Point	X coordinate	Y coordinate
1	0	2.953
2	0.61	2.9310
3	1.215	2.861
4	1.931	2.696
5	3.089	2.11
6	3.871	1.194
7	-0.61	2.9310
8	-1.215	2.861
9	-1.931	2.696
10	-1.089	2.11
11	-3.871	1.194

Table A.4: Fourth oval's points in LEle laboratory.

Point	X coordinate	Y coordinate
1	0	-3.827
2	0.61	-3.801
3	1.215	-3.72
4	1.47	-3.668
5	1.931	-3.543
6	3.089	-3.013
7	-0.61	-3.801
8	-1.215	-3.72
9	-1.47	-3.668
10	-1.931	-3.543
11	-3.089	-3.013

Table A.5: Fifth oval's points in LEle laboratory.

Point	X coordinate	Y coordinate
1	0	-4.4
2	0.61	-4.373
3	1.215	-4.291
4	1.47	-4.239
5	1.931	-4.117
6	3.089	-3.62
7	-0.61	-4.373
8	-1.215	-4.291
9	-1.47	-4.239
10	-1.931	-4.117
11	-3.089	-3.62

Table A.6: Sixth oval's points in LEle laboratory.

Point	X coordinate	Y coordinate
1	0	-6
2	0.61	-5.975
3	1.215	-5.903
4	1.47	-5.856
5	1.931	-5.748
6	3.089	-5.335
7	-0.61	-5.975
8	-1.215	-5.903
9	-1.47	-5.856
10	-1.931	-5.748
11	-3.089	-5.335

A.2   Garage of DEI

In this section, all the Cartesian coordinates of the measured points in DEI's Garage are presented.

Table A.7: First oval's points in DEI's Garage.

Point	X coordinate	Y coordinate
1	0	0.5
2	0.5038	0.6605
3	1.016	0.8747
4	1.506	0.946
5	2.002	0.8247
6	2.251	0.6454
7	-0.5038	0.6605
8	-1.016	0.8747
9	-1.506	0.946
10	-2.002	0.8247
11	-2.251	0.6454

Table A.8: Second oval's points in DEI's Garage.

Point	X coordinate	Y coordinate
1	0	1.3
2	0.5006	1.324
3	0.9921	1.356
4	1.512	1.328
5	2.008	1.179
6	2.255	1.032
7	-0.5006	1.324
8	-0.9921	1.356
9	-1.512	1.328
10	-2.008	1.179
11	-2.255	1.032

Table A.9: Third oval's points in DEI's Garage.

Point	X coordinate	Y coordinate
1	0	2
2	0.5083	1.991
3	1.02	1.952
4	1.508	1.865
5	2.012	1.692
6	2.496	1.393
7	-0.5083	1.991
8	-1.02	1.952
9	-1.508	1.865
10	-2.012	1.692
11	-2.496	1.393

Table A.10: Fourth oval's points in DEI's Garage.

Point	X coordinate	Y coordinate
1	0	3.2
2	1.003	3.113
3	2.012	2.818
4	2.501	2.571
5	3.012	2.2
6	3.507	1.655
7	-1.003	3.113
8	-2.012	2.818
9	-2.501	2.571
10	-3.012	2.2
11	-3.507	1.655

Table A.11: Fifth oval's points in DEI's Garage.

Point	X coordinate	Y coordinate
1	0	4.4
2	1.003	4.316
3	1.999	4.053
4	3.002	3.562
5	3.999	2.717
6	4.501	2.02
7	-1.003	4.316
8	-1.999	4.053
9	-3.002	3.562
10	-3.999	2.717
11	-4.501	2.02

Table A.12: Sixth oval's points in DEI's Garage.

Point	X coordinate	Y coordinate
1	0	5.7
2	1.003	5.626
3	2.003	5.4
4	3.007	4.997
5	4.004	4.373
6	4.999	3.402
7	-1.003	5.626
8	-2.003	5.4
9	-3.007	4.997
10	-4.004	4.373
11	-4.999	3.402

Appendix B

Example of the intermediate processing steps in DEI's Garage

In the same manner as explained in Chapter 3, the processing of the Garage's gathered signal samples starts by calculating the average of the ER waveforms as presented in Figure B.1.
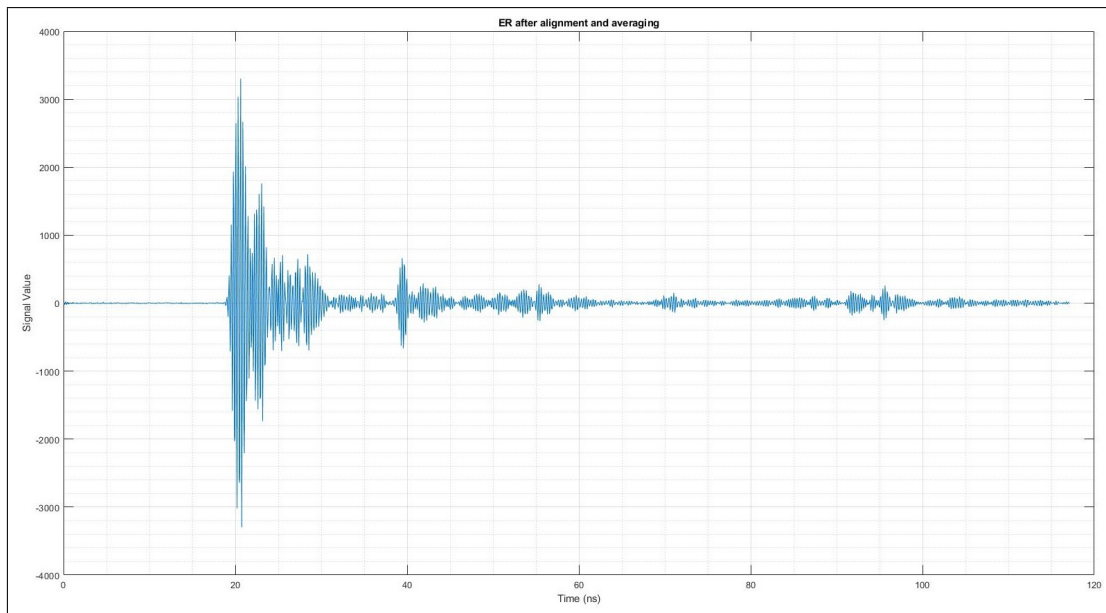

Figure B.1: Garage's ER signal after alignment and averaging.

Using the same procedure, the alignment and averaging code was applied to all the points in the experiment and in Figure B.2
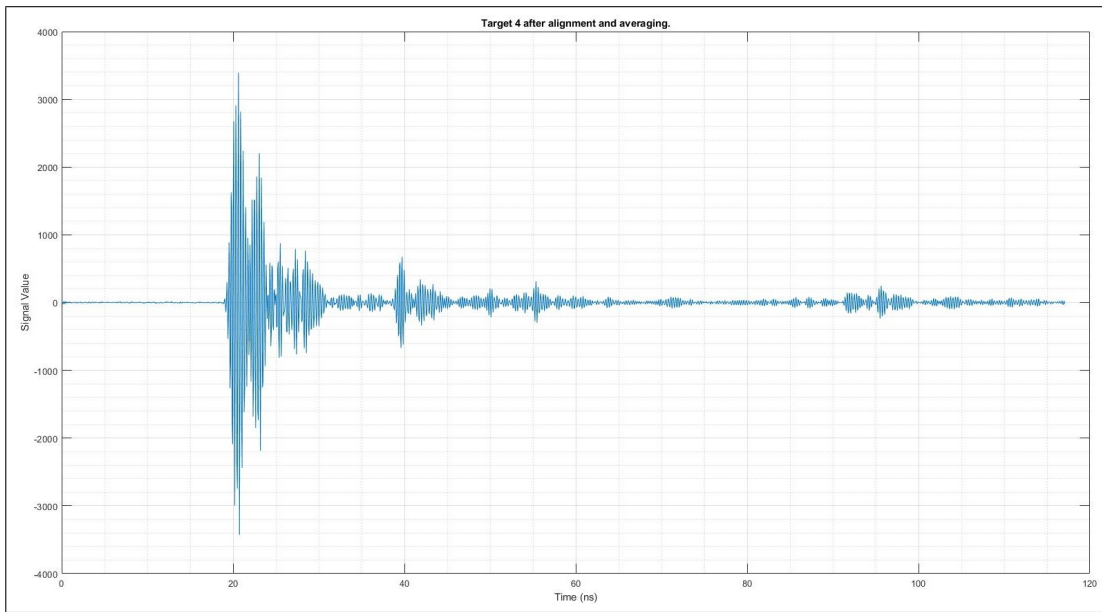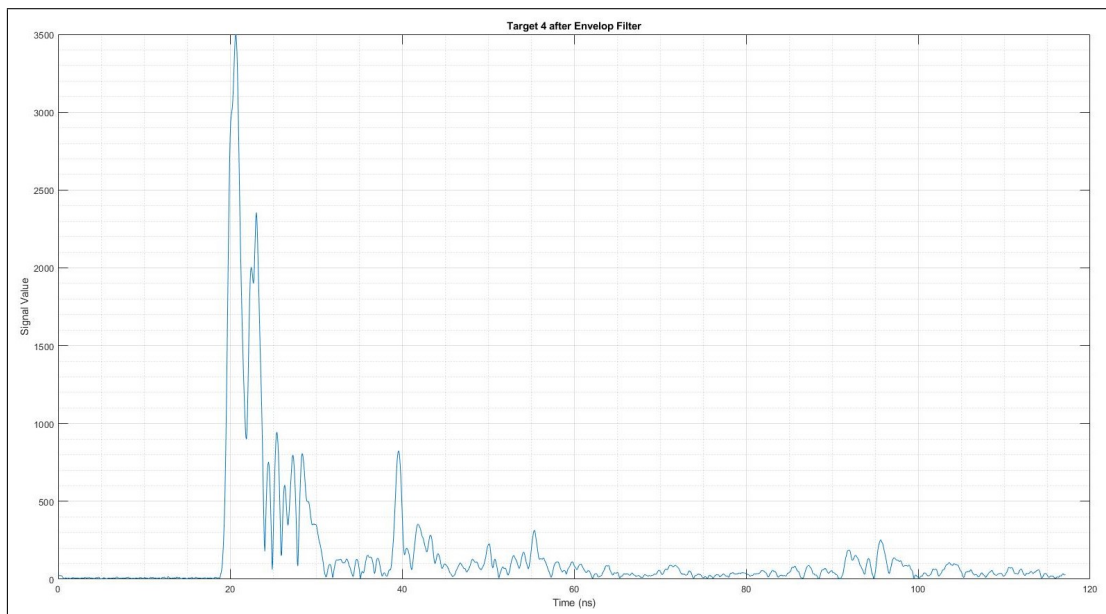
Figure B.2: Garage's Target #4 in oval #1 signal after alignment and averaging.

With both, the ER signal and the target's information aligned and averaged, the next step is to filter them to extract the envelop. The result of this step is shown in Figures B.3 and B.4, respectively.
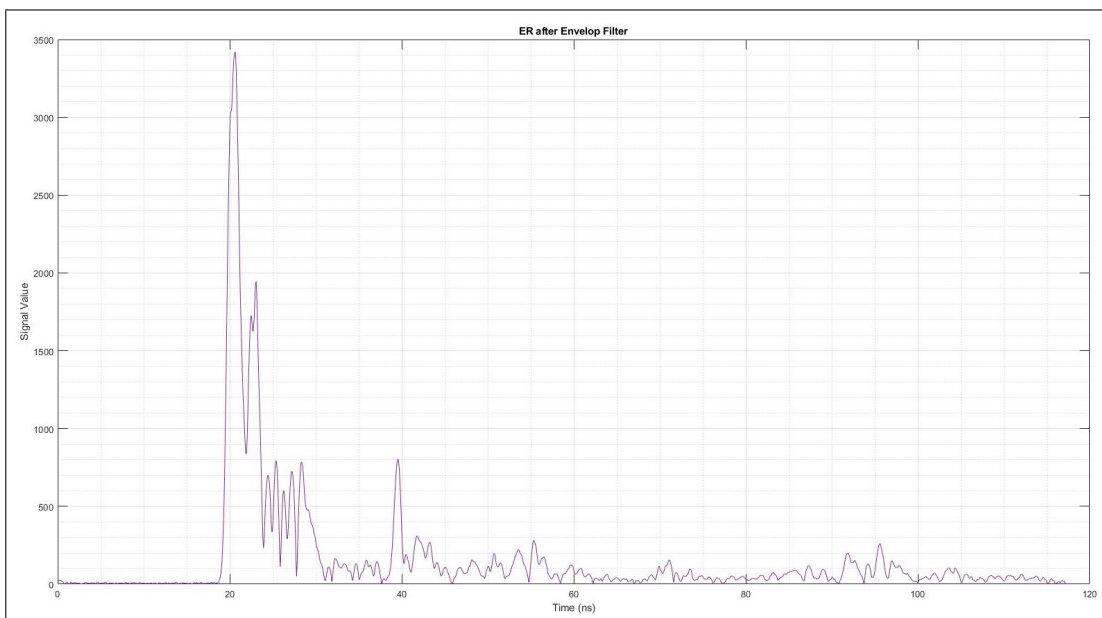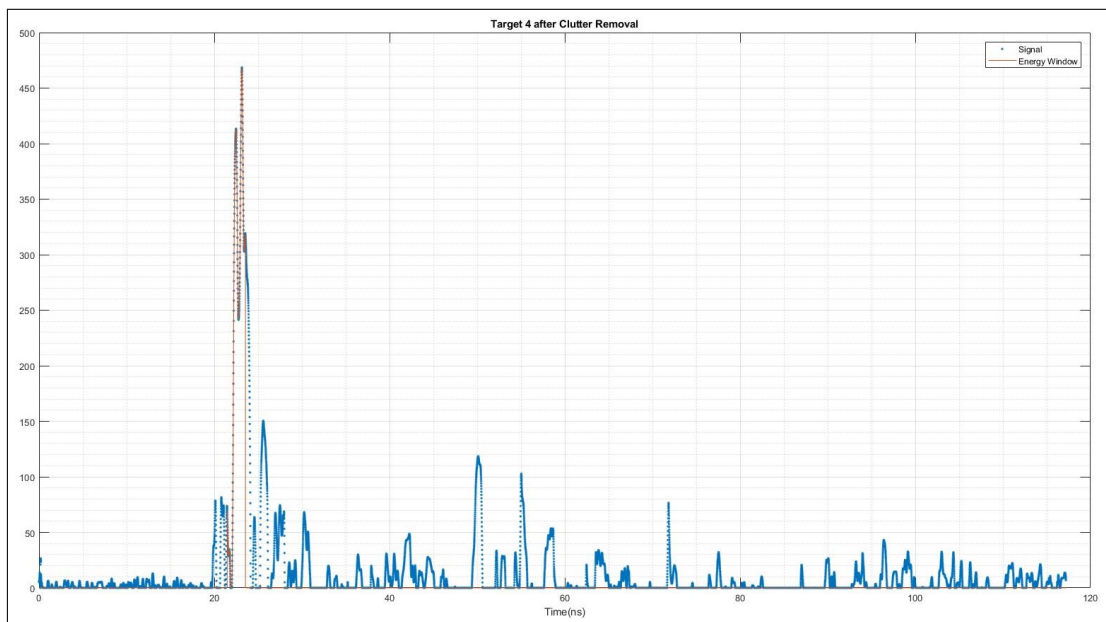

**Figure B.3:** Garage's ER signal after envelop extraction.

Figure B.4: Garage's Target #4 in oval #1 signal after envelop extraction.

With the filtered signals prepared, the difference between them is calculated, then this result is rectified to set all the negative values to zero and the "clutter free" waveform is obtained. This result is presented in Figure B.5.
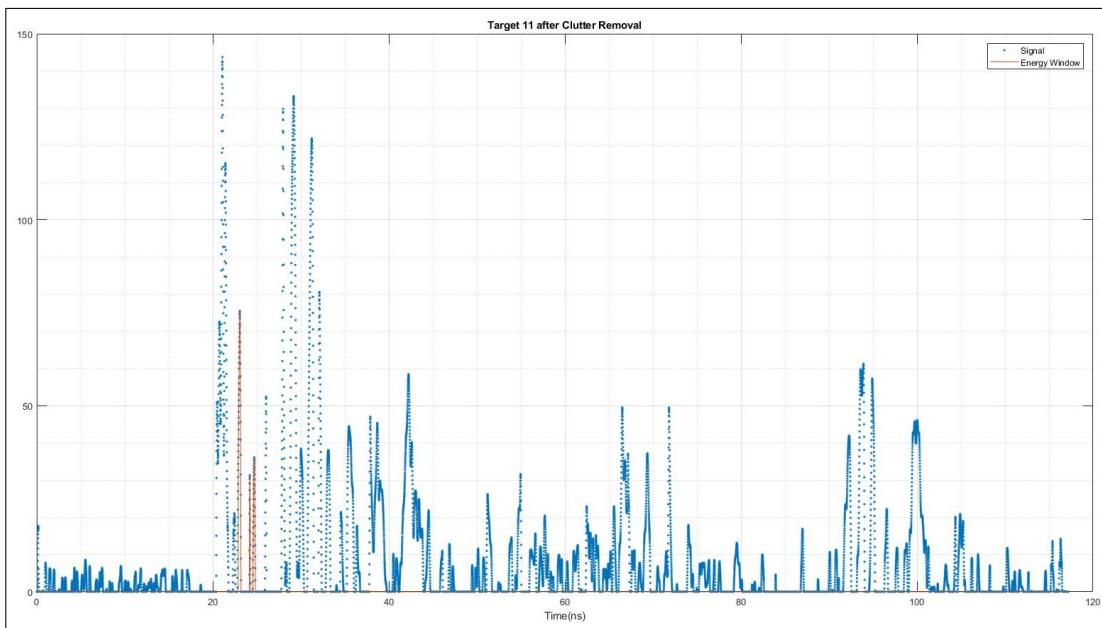

Figure B.5: Garage's Target #4 in oval #1 signal after clutter removal.

The DEI's Garage "clutter free" signals showed similar behavior as the LEle laboratory in the sense that it is not always clear the target's contributions in the waveform (refer to Figures B.6 and B.7).
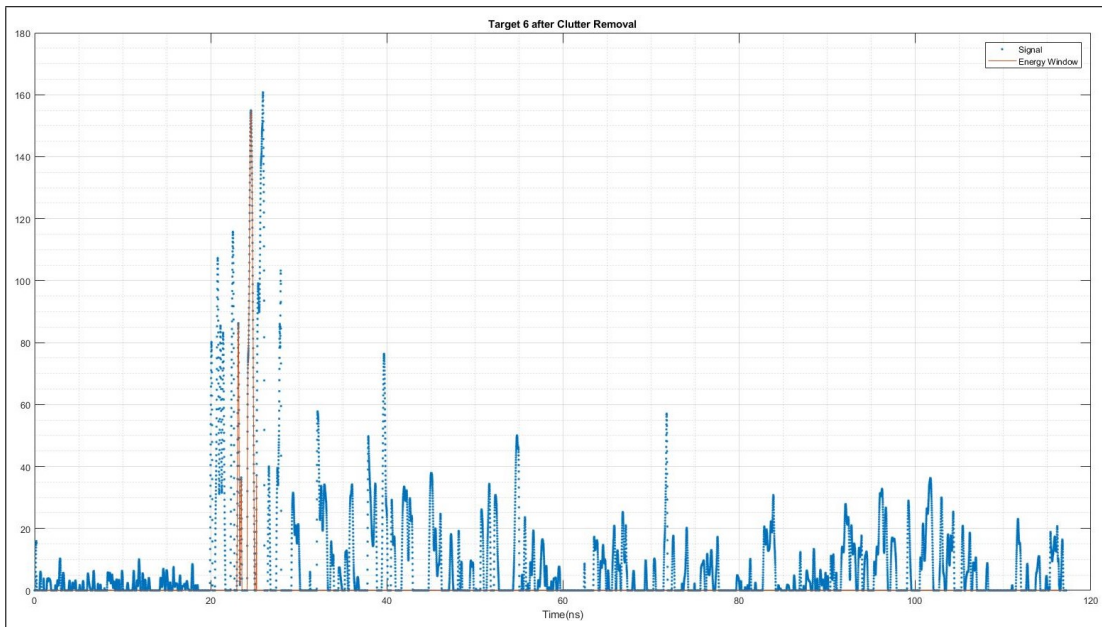
Figure B.6: Garage's Target #6 in oval #1 signal after clutter removal.

Figure B.7: Garage's Target #11 in oval #1 signal after clutter removal.

Once again, the influence of objects in the room with similar values of $L_1 \cdot L_2$ as the target's affect in constructive and destructive forms the obtained result after the clutter removal process. Remember, there is no deterministic procedure to account for these effects but the methodology used in this thesis exhibited accurate results.